

**Anisotropic and pressure tunable magnetism of titanium-based Kagome ferromagnet
SmTi₃Bi₄**

Long Chen (陈龙)^{1, 2, #}, Ying Zhou (周颖)^{1, 2, #}, He Zhang (张赫)^{1, 2, #}, Zhongnan Guo (郭中楠)³,
Xiaohui Yu (于晓辉)^{1, 2, 4, *}, Gang Wang (王刚)^{1, 2, 4, *}

¹ Beijing National Laboratory for Condensed Matter Physics, Institute of Physics, Chinese
Academy of Sciences, Beijing 100190, China

² University of Chinese Academy of Sciences, Beijing 100049, China

³ Department of Chemistry, School of Chemistry and Biological Engineering, University of
Science and Technology Beijing, Beijing 100083, China

⁴ Songshan Lake Materials Laboratory, Dongguan, Guangdong 523808, China

These authors contributed equally to this work.

*Corresponding author. Email: yuxh@iphy.ac.cn; gangwang@iphy.ac.cn.

Abstract

Kagome magnets showing diverse topological quantum responses are crucial for next-generation topological engineering. Here we report the physical properties of a newly discovered titanium-based Kagome ferromagnet SmTi₃Bi₄, mainly focusing on its anisotropy and high-pressure tunability of magnetism. The crystal structure of SmTi₃Bi₄ belongs to the RETi₃Bi₄ (RE = Rare earth element) prototype, featuring a distorted Ti Kagome lattice in TiBi layer and Sm-atomic zig-zag chain along the *c* axis. By the temperature-dependent resistivity, heat capacity, and magnetic susceptibility measurements, a ferromagnetic (FM) ordering temperature T_c is determined to be 23.2 K, above which a *T*-linear resistivity and quite large density of states near Fermi level are hinted to exist. A large magnetic anisotropy was observed by rotating the in-plane magnetic field, showing the *b* axis is the easy magnetizations axis. The resistance under high pressure shows a suppression from 23.2 K to 8.5 K up to 23.5 GPa first and a following little enhancement up to 44.8 GPa. Considering the large in-plane magnetization between stacked Kagome lattices and tunability of FM order, possible topological phase transitions can be anticipated in SmTi₃Bi₄, which should be a new promising platform to explore the complex electronic and magnetic phases based on Kagome lattice.

Introduction

Due to the strong geometric frustration [1] and nontrivial band topology [2], Kagome lattice has been acting as a fertile platform to investigate the quantum interactions between geometry, topology, spin, and correlation [3]. Nonmagnetic Kagome materials have already attracted tremendous attention owing to the existence of superconductivity [4-8], charge density wave [9-11], nontrivial topological states [12], possible fractionalization [13] and Fermi surface instabilities [14]. With the combination of magnetism, Kagome magnets with magnetic ordering would naturally support the tunability of their exotic properties through magnetism, which would result in abundant topological phases and quantum responses [15, 16]. Over the past decade, rich emergent quantum phenomena, including anomalous Hall effects [16-19], anomalous Nernst effects [20-23], negative magnetoresistance from chiral anomaly [24], nontrivial topological states [25-28], charge density waves [29, 30] and so on, have emerged in Kagome magnets. Due to the possible tunability of magnetism under a magnetic field or other controllable parameters, topological Kagome magnets are anticipated to engender highly tunable topological states [15, 16, 27], which is crucial for next-generation topological engineering.

By introducing different rare-earth elements inter-between stacked Kagome lattice, various magnetic orderings along with different quantum transport behaviors have been observed in Kagome magnets, typically exemplified as $RE\text{Mn}_6\text{Sn}_6$ [16, 31, 32], $RE\text{V}_6\text{Sn}_6$ [33, 34], $RE\text{V}_3\text{Sb}_4$ [35] and recently discovered $RE\text{Ti}_3\text{Bi}_4$ [36], where RE is a rare-earth element. Due to the coexisting magnetism induced by Mn Kagome lattice and RE atoms, the magnetic ground states of $RE\text{Mn}_6\text{Sn}_6$ range from different ferrimagnetic states (RE = Gd-Ho) [32, 37] to antiferromagnetic (AFM) order (RE = Er, Tm, and Lu) [32]. By contrast, as the V/Ti Kagome lattices appear to be nonmagnetic, the RE atoms would dominate the magnetism and result in various magnetic states, including nonmagnetic/paramagnetic $Er/\text{TmV}_6\text{Sn}_6$ [33], YbTi_3Bi_4 [36] and YbV_3Sb_4 [35], AFM $RE\text{V}_6\text{Sn}_6$ (Gd-Ho) [33, 34] and CeTi_3Bi_4 [38], possible short-ranged PrTi_3Bi_4 and ferromagnetic (FM) TbV_6Sn_6 [39, 40], EuV_3Sb_4 [35] and NdTi_3Bi_4 [36]. Among them, the Kagome ferromagnets with either in-plane or out-of-plane magnetization have attracted most of attention due to their potential of hosting Chern gaps or tunable topological phases. However, Kagome ferromagnets is still little studied and it is quite essential to discover new topological Kagome ferromagnets and explore their properties.

In this work, we present the single crystal growth, characterization of the anisotropy and high-pressure tunability of magnetism in a new Kagome ferromagnet, SmTi_3Bi_4 . Similar to $RE\text{V}_3\text{Sb}_4$ and $RE\text{Ti}_3\text{Bi}_4$, SmTi_3Bi_4 contains a distorted and nonmagnetic Ti Kagome lattice and quasi-one dimensional Sm-atomic zig-zag chain. Owing to the magnetism dominated by Sm, a FM order with $T_c = 23.2$ K are hints to exist according to the temperature-dependent resistivity, heat capacity and magnetic susceptibility. By varying the directions of applying magnetic field, both large out-of-plane and in-plane anisotropy of magnetism are observed, showing the b -axis is the easy axis. Exotic topological phases are anticipated in this stacked Kagome materials with large in-plane magnetization. The high-pressure tunability of the FM order is confirmed by the resistance measurement under high pressure up to 44.8 GPa, hinting potentially controllable parameters to tune

the magnetism and corresponding band topology. Our results further expands the known Kagome magnets, providing a new platform to explore the complex electronic and magnetic phases based on Kagome lattice.

Results and Discussion

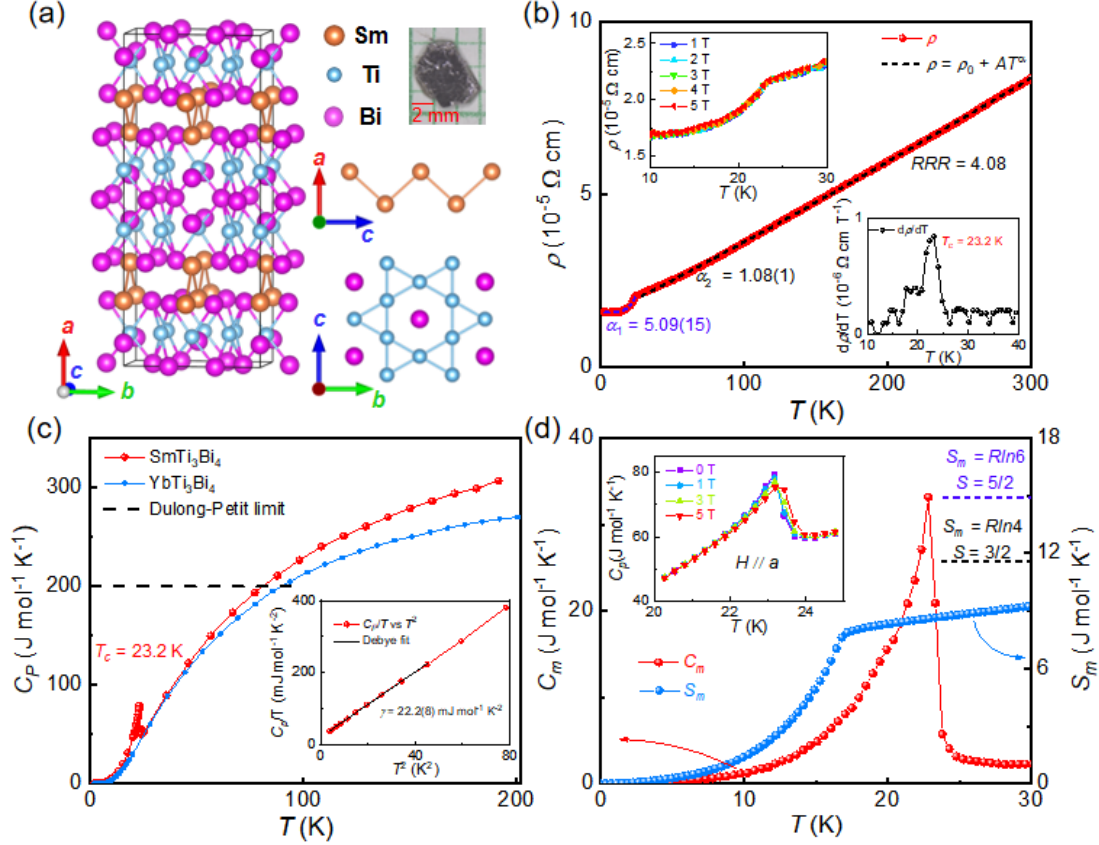


Figure 1. Crystal structure and phase transition of SmTi₃Bi₄ single crystal. (a) Crystal structure of SmTi₃Bi₄, containing Sm-atomic zig-zag chain viewed along the *b* axis and Ti Kagome lattice in TiBi layer viewed along the *a* axis. Upper right part shows an optical photograph of an as-grown single crystal with a grid size of 2 mm. (b) Temperature-dependent in-plane resistivity of SmTi₃Bi₄ single crystal with current in the *bc* plane ($I // bc$). The dashed lines show the power law fittings. Upper inset shows the temperature-dependent resistivity under out-of-plane magnetic field (1 T - 5 T). Lower inset shows the first derivative of resistivity ($d\rho/dT$). (c) Temperature-dependent specific heat capacity of SmTi₃Bi₄. The specific heat capacity of nonmagnetic YbTi₃Bi₄ is taken as reference. The inset shows C_P vs T^2 plot and corresponds fittings (black lines) using Debye model. (d) Specific heat capacity contributed by magnon (C_m) and corresponding magnetic entropy (S_m). The dashed lines are theoretical saturated magnetic entropy with different spin states ($S = 5/2$ or $3/2$). The inset shows the specific heat capacity of SmTi₃Bi₄ under different out-of-plane magnetic field (1 T - 5 T).

SmTi₃Bi₄ crystallizes in an orthogonal space group $Fm\bar{3}m$ (No.69) with $a = 24.900(4) \text{ \AA}$, $b = 10.3371(16) \text{ \AA}$, $c = 5.8863(9) \text{ \AA}$, and $\alpha = \beta = \gamma = 90^\circ$ (Table S1-S4, Figure S1). It contains the similar structural motif as that of REV₃Sb₄ (RE = Yb, Eu) [35] and RET₃Bi₄ (RE = La-Nd, Yb) [36], featuring Sm-atomic zig-zag chain and distorted Ti Kagome lattice (Figure 1a). Figure 1b shows

the temperature-dependent in-plane resistivity of SmTi₃Bi₄, where the residual-resistance ratio ($RRR = \rho_{300\text{ K}}/\rho_{25\text{ K}}$) is calculated to be 4.08, suggesting a good crystallinity of SmTi₃Bi₄ single crystal. With current (2 mA) being applied in the bc plane ($I // bc$), the resistivity monotonically decreases with decreasing of temperature, showing a metallic-like behavior with an obvious drop around $T_c = 23.2$ K. The resistivity can be fitted using the power law: $\rho = \rho_0 + AT^\alpha$, where the value of power α is dependent on the dominant scattering mechanism. Usually, α takes the value of 3/2 for diffusive electron motion caused by strong electron correlation [41], 2 for Fermi liquid with moderate electron-electron scattering [42, 43], 3 for dominant s - d scattering or electron-magnon scattering [44, 45], and 5 for electron-phonon coupling [46]. Below T_c , the resistivity is fitted using the power law with $\alpha_1 = 5.09(15)$, showing strong electron-phonon coupling. Above T_c , the resistivity shows a clear non-Fermi liquid behavior with $\alpha_2 = 1.08(1)$, implying a linear-in-temperature (T -linear) resistivity which is usually associated with quantum critical physics and unconventional superconductivity [47-49]. Compared with other RE Ti₃Bi₄ (RE = Yb, Pr, and Nd) [36], the smallest value of power α and the highest transition temperature of SmTi₃Bi₄ suggests that stronger electron correlation corresponds to higher ordering temperature. Upon applying an out-of-plane magnetic field, the resistivity and the transition temperature hardly changes with magnetic field increased from 1 T to 5 T, showing a possible FM order.

Compared with nonmagnetic YbTi₃Bi₄, the temperature-dependent specific heat capacity of SmTi₃Bi₄ single crystal shows a clear λ -shape peak at $T_c = 23.2$ K (Figure 1c). At high temperature, the specific heat capacity of SmTi₃Bi₄ single crystals exceeds the Dulong–Petit limit ($3NR \sim 200$ J mol⁻¹ K⁻¹, black dashed line), which is attributed to the more prominent phonon contribution at higher temperature of N-type grease used for protecting the samples. By fitting the low-temperature (2 K - 6 K) specific heat capacity using Debye model, the Sommerfeld coefficient γ proportional to the density of states (DOSs) around Fermi level (E_F) ($\gamma \propto g(E_F)$) [50] is determined to be 22.2(8) mJ K⁻² per formula for SmTi₃Bi₄, which is close to that of YbTi₃Bi₄ (20.7(7) mJ K⁻² per formula) [36]. Above T_c , quite large DOSs near E_F are hinted to exist with $\gamma = 1679.7(4.3)$ mJ K⁻² per formula (Figure S2), which may be related with strong electron correlation represented by the linear dependence of resistivity. Taking the specific heat capacity of nonmagnetic YbTi₃Bi₄ containing electron and phonon contributions as a reference, the specific heat capacity only contributed by magnon (C_m) and corresponding magnetic entropy (S_m) of SmTi₃Bi₄ are determined (Figure 1d). The saturated magnetic entropy is calculated to be 9.24 J mol⁻¹ K⁻¹ at 30 K, reaching about 79.9% of the theoretical value for $S = 3/2$ ($R \ln(2S+1) = 11.56$ J mol⁻¹ K⁻¹) and only 61.8% of that for $S = 5/2$ ($R \ln(2S+1) = 14.95$ J mol⁻¹ K⁻¹), which may suggest a reduction from the highest spin state of Sm³⁺ owing to the crystal field effect. Upon applying an out-of-plane magnetic field, the peak slightly shifts to higher temperature up to 5 T, further suggesting a FM order.

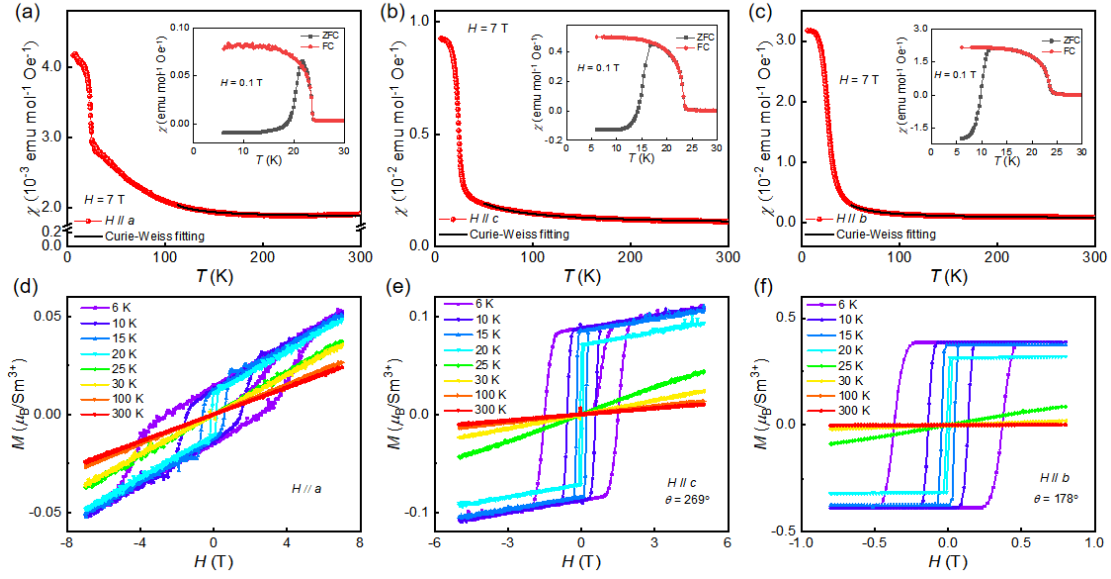


Figure 2. Ferromagnetic order in SmTi_3Bi_4 single crystal. Temperature-dependent magnetic susceptibility of SmTi_3Bi_4 with large magnetic field (7 T) parallel to the (a) a axis ($H \perp bc$), (b) c axis ($H // bc$, $\theta = 269^\circ$), and (c) b axis ($H // bc$, $\theta = 178^\circ$). The black lines are Curie-Weiss fitting curves. The insets show the corresponding ZFC and FC curves under a small magnetic field (0.1 T). Field-dependent magnetization curves at different temperature of SmTi_3Bi_4 under magnetic field parallel to the (d) a axis, (e) c axis, and (f) b axis.

Figure 2a-c shows the magnetic susceptibility of SmTi_3Bi_4 single crystal with applied magnetic field parallel to the a axis, c axis and b axis, respectively (See Figure S3 for details of crystal orientation). Under a small magnetic field (0.1 T), a bifurcation between the zero-field-cooling (ZFC) and field-cooling (FC) curves can be clearly resolved at low temperature with magnetic susceptibility sharply increasing around $T_c = 23.2$ K, suggesting a possible FM order. Under a large magnetic field (7 T), the magnetic susceptibility increases and shows a sudden enhancement around T_c upon cooling, whereas follows the Curie-Weiss law $\chi = \chi_0 + C/(T - \theta)$ at high temperature (black lines), where χ_0 is the temperature-independent contribution including the diamagnetic contribution of the orbital magnetic moment, C the Curie constant, and θ the Curie temperature. The fitted Curie temperatures for $H // a$ and $H // b$ are large and positive (85 K for $H // a$ and 23 K for $H // b$), showing strong FM interactions. For $H // c$, the fitted Curie temperature is negative and close to zero (-3 K), indicating the possible competition between FM and AFM interaction. Following the equation $\mu_{\text{eff}} = \sqrt{\frac{8C}{n}}$, where n is the number of magnetic atoms, the effective moments are calculated to be $0.20(3) \mu_B$ for $H // a$, $0.71(1) \mu_B$ for $H // b$, and $0.64(1) \mu_B$ for $H // c$, respectively. In particular, the effective moment for $H // b$ is quite close to the theoretical effective moment of Sm^{3+} ($0.84 \mu_B$). According to the value of magnetic susceptibility under 7 T at 6 K, $\chi_{H // b}$ ($3.2 \times 10^{-2} \text{ emu mol}^{-1} \text{ Oe}^{-1}$) $>$ $\chi_{H // c}$ ($0.9 \times 10^{-2} \text{ emu mol}^{-1} \text{ Oe}^{-1}$) $>$ $\chi_{H // a}$ ($4.2 \times 10^{-3} \text{ emu mol}^{-1} \text{ Oe}^{-1}$), the easy plane is the bc plane and the easy axis is along the b axis. The FM ordering happened at T_c is firmly confirmed by the field-dependent magnetization curves, where obvious hysteresis loops

exist at low temperature and gradually vanish as temperature increases beyond T_c (Figure 2d-f). For $H \parallel b$, the smaller coercive magnetic field ($H_{c_b//} \sim 0.5 \text{ T} < H_{c_c//} \sim 2.5 \text{ T} < H_{c_a//} \sim 5 \text{ T}$) and larger saturation moment ($\mu_{\text{sat_}b//} \sim 0.5 \mu_B > \mu_{\text{sat_}c//} \sim 0.1 \mu_B > \mu_{\text{sat_}a//} \sim 0.05 \mu_B$) further indicate that the easy axis is the b axis. The large out-of-plane and in-plane anisotropy should come from the quasi-two dimensional structure and quasi-one dimensional Sm-atomic zig-zag chain.

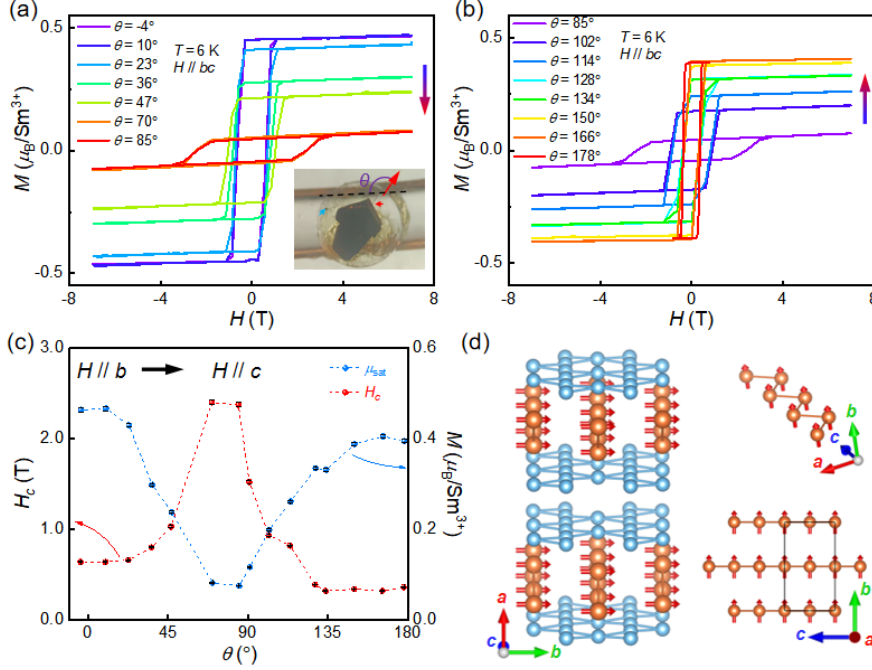


Figure 3. In-plane magnetic anisotropy of SmTi_3Bi_4 single crystal. Field-dependent magnetization curves ($T = 6 \text{ K}$) of SmTi_3Bi_4 under in-plane magnetic field ranging from (a) $\theta = -4^\circ$ to $\theta = 85^\circ$ and (b) $\theta = 85^\circ$ to $\theta = 178^\circ$. The inset of (a) shows the measurement geometry with θ representing the angle between the b axis and magnetic field. (c) Evolution of saturation moment and coercive magnetic field with the direction of in-plane magnetic field. (d) Schematic picture of FM ordering in SmTi_3Bi_4 . Only Sm atoms in the zig-zag chain and Ti-Kagome lattice are shown for clarity.

Considering the in-plane magnetic anisotropy of SmTi_3Bi_4 , the field-dependent magnetization curves are measured at 6 K under in-plane magnetic field with different directions (Figure 3a-b). With the angle between b axis and magnetic field (θ) ranging from -4° to 85° , the coercive magnetic field monotonically increases and the saturation moment monotonically decreases, whereas the coercive magnetic field monotonically decreases and the saturation moment monotonically increases with θ ranging from 85° to 178° (Figure 3c). The evolution of coercive magnetic field and saturation moment fits in a two-fold symmetry, which is consistent with the orthogonal crystal structure. Considering the b axis as the easy axis and FM ordering below T_c , Sm-atomic zig-zag chains with large in-plane magnetization sandwiched by Ti-Kagome lattices (Figure 3d), which is anticipated to induce tunable topological phases because the large in-plane magnetization would close the gaps in topological Kagome magnets. Similar scenarios, where long ranger magnetic order on a low dimensional lattice sandwiched by topological lattices has recently been predicted or

observed in other systems, like magnetism-tuned topological phases in square-net compound ErAsS with exotic hourglass surface states [51] or anomalous Hall conductivity in possible Chern insulator TbV₆Sn₆ [40].

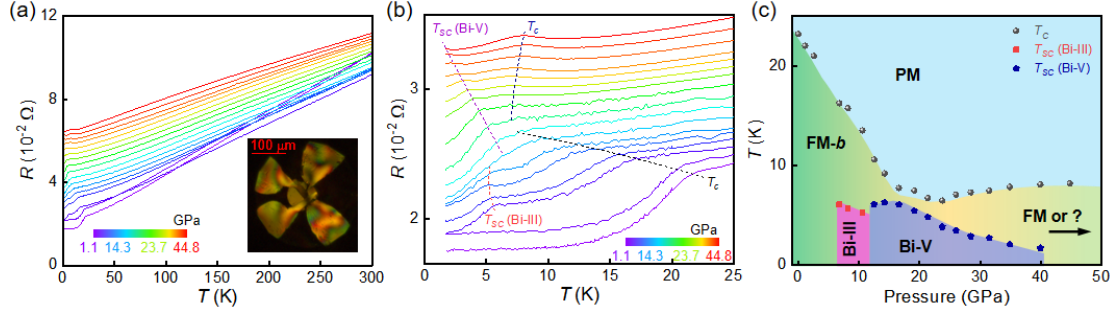


Figure 4. Magnetism tuned by pressure. (a) Temperature-dependent resistance of SmTi_3Bi_4 under high pressure ranging from 1.1 GPa to 44.8 GPa. The inset shows the optical photograph of four probe configuration in the diamond-anvil cell. (b) Resistance at low temperature ranging from 1.7 K to 25 K. The dashed lines show the evolution trend of FM ordering temperature (T_c) and possible superconducting transition temperature (T_{SC}). The resistance data in (a) and (b) are relatively offset for clarity. (c) Pressure dependence of T_c and possible T_{SC} . The shaded areas denote different magnetic or possible superconducting phases.

To explore the possible superconductivity and evolution of magnetism under high pressure, *in situ* high-pressure resistance of SmTi_3Bi_4 were measured under pressure up to 44.8 GPa by using a diamond-anvil cell (**Figure 4a**). All the resistance curves exhibit typical metallic feature beyond T_c with RRR ($R_{300\text{ K}}/R_{25\text{ K}}$) reduced from 4.22 at 1.1 GPa to 2.51 at 44.8 GPa, indicating a weakening of metallicity as the pressure increase. Beside the drop related to FM ordering, another downward drop shows up in resistance at lower temperature as pressure goes beyond 6.8 GPa, resulting in two successive drops in resistance curves. The higher temperature drop representing the FM ordering temperature is gradually suppressed from 22.0 K at 1.1 GPa to 6.5 K at 23.7 GPa, whereas the lower temperature drop is suppressed with a sudden jump at 12.5 GPa. As pressure goes beyond 23.7 GPa, the higher temperature drop shifts to an resistance enhancement around 7.5 K (Figure S5a) and the maximum moves a little to higher temperature as the pressure increases, whereas the lower temperature drop is suppressed down below 1.8 K at 40.0 GPa (Figure 4b). By applying external magnetic field, the drop or enhancement at higher temperature hardly changes but the drop at lower temperature is always suppressed (Figure S5b-d), indicating a FM ordering at higher temperature (T_c) and a possible superconducting transition at lower temperature (T_{SC}), respectively. Considering the similar value and evolution of superconducting transition temperature with that of Bi under pressure [36, 52] and Bi-rich nature of SmTi_3Bi_4 (50%), the anomaly at low temperature might come from the remaining Bi-flux droplets or Bi side phase generated under pressure as observed in NdTi_3Bi_4 [36]. Unlike NdTi_3Bi_4 , the FM order of SmTi_3Bi_4 can be always clearly resolved owing to the relatively larger difference between the T_c of SmTi_3Bi_4 and possible T_{SC} of pressurized Bi. Anyhow, the FM order of SmTi_3Bi_4 is suppressed from 23.2 K to 6.5 K under 23.7 GPa first, and

then seems to be little enhanced under higher pressure up to 44.8 GPa. The sensitivity of FM order to pressure hints that chemical doping and strain or stress would be effective parameters to tune the magnetism and corresponding electronic topology of SmTi_3Bi_4 . Whether the enhanced temperature corresponds to another magnetic transition and potential superconducting transition temperature at further higher pressure still need systematic investigations. Considering the Bi-rich feature, new RETi_3Bi_4 (RE = rare earth element) compounds with higher ordering temperature are expected to avoid the overlap between its ordering and the superconducting transition of pressurized Bi under pressure.

Conclusion

New titanium-based Kagome ferromagnet SmTi_3Bi_4 has been discovered, which has crystal structure belongs to the RETi_3Bi_4 (RE = Rare earth element) prototype, featuring distorted Ti-Kagome lattice in TiBi layer and Sm-atomic zig-zag chain along the c axis. A clear FM transition is observed at $T_c = 23.2$ K, along with a T -linear resistivity and quite large DOSs near E_F above T_c . According to the large magnetic anisotropy, the magnetic moments tend to align along the b axis. Thus, Sm-atomic zig-zag chains with large in-plane magnetization are sandwiched by Ti Kagome lattices, which is anticipated to induce exotic topological phase transitions. By applying pressure, the FM order is suppressed from 23.2 K to 8.5 K under 23.5 GPa, and then enhanced a little under pressure up to 44.8 GPa. The results not only report a new titanium-based Kagome magnets SmTi_3Bi_4 with the up-to-date highest FM ordering temperature ($T_c = 23.2$ K) among RETi_3Bi_4 (RE = Yb, La-Nd, Sm), but also manifest its tunability under pressure.

Acknowledgments

L. Chen, Y. Zhou, and H. Zhang contributed equally to this work. L. Chen, Y. Zhou and G. Wang would like to thank Prof. X. L. Chen, Prof. J. P. Hu, Prof. H. M. Weng, Prof. T. Qian at Institute of Physics, Chinese Academy of Sciences, and Prof. J. Ma at Shanghai Jiao Tong University for helpful discussions. This work was partially supported by the National Key Research and Development Program of China (Grant Nos. 2018YFE0202600 and 2022YFA1403900) and the National Natural Science Foundation of China (Grant Nos. 51832010 and 11888101).

Author contributions

G. Wang, X.L. Chen, and X.H. Yu conceived the idea. L. Chen and Y. Zhou grew the single crystals, performed the characterization of crystal structure, transport properties, and magnetism. H. Zhang conducted the high-pressure measurement of resistivity. Z.N. Guo helped in the refinement of single crystal X-ray diffraction data. L. Chen and G. Wang wrote the manuscript with contributions from all other authors.

Declaration of interests

The authors declare no competing financial interest.

Supporting information

Materials and methods; Crystal structure and chemical composition (Table S1-S4, Figure S1); Magnetism and specific heat capacity; (Table S5, Figure S2-S4); Resistance under high pressure (Figure S5).

Supporting Information is available online or from the corresponding author.

Reference

- [1] J. Strečka, L. Čanová, M. Jaščur, M. Hagiwara, Exact solution of the geometrically frustrated spin-1/2 Ising-Heisenberg model on the triangulated kagome (triangles-in-triangles) lattice, *Phys. Rev. B*, 78 (2008) 024427.
- [2] H.M. Guo, M. Franz, Topological insulator on the kagome lattice, *Phys. Rev. B*, 80 (2009) 113102.
- [3] J.-X. Yin, B. Lian, M.Z. Hasan, Topological kagome magnets and superconductors, *Nature*, 612 (2022) 647-657.
- [4] W.-H. Ko, P.A. Lee, X.-G. Wen, Doped kagome system as exotic superconductor, *Phys. Rev. B*, 79 (2009) 214502.
- [5] S.-L. Yu, J.-X. Li, Chiral superconducting phase and chiral spin-density-wave phase in a Hubbard model on the kagome lattice, *Phys. Rev. B*, 85 (2012) 144402.
- [6] B.R. Ortiz, S.M.L. Teicher, Y. Hu, J.L. Zuo, P.M. Sarte, E.C. Schueller, A.M.M. Abeykoon, M.J. Krogstad, S. Rosenkranz, R. Osborn, R. Seshadri, L. Balents, J. He, S.D. Wilson, CsV₃Sb₅: A Z₂ topological Kagome metal with a superconducting ground state, *Physical Review Letters*, 125 (2020) 247002.
- [7] B.R. Ortiz, P.M. Sarte, E.M. Kenney, M.J. Graf, S.M.L. Teicher, R. Seshadri, S.D. Wilson, Superconductivity in the Z₂ kagome metal KV₃Sb₅, *Phys. Rev. Materials*, 5 (2021) 034801.
- [8] Q.W. Yin, Z.J. Tu, C.S. Gong, Y. Fu, S.H. Yan, H.C. Lei, Superconductivity and normal-state properties of Kagome metal RbV₃Sb₅ single crystals, *Chin. Phys. Lett.*, 38 (2021) 037403.
- [9] S. Cho, H. Ma, W. Xia, Y. Yang, Z. Liu, Z. Huang, Z. Jiang, X. Lu, J. Liu, Z. Liu, J. Li, J. Wang, Y. Liu, J. Jia, Y. Guo, J. Liu, D. Shen, Emergence of new van Hove singularities in the charge density wave state of a topological Kagome metal RbV₃Sb₅, *Physical Review Letters*, 127 (2021) 236401.
- [10] Y. Song, T. Ying, X. Chen, X. Han, X. Wu, A.P. Schnyder, Y. Huang, J. Guo, X. Chen, Competition of Superconductivity and Charge Density Wave in Selective Oxidized CsV₃Sb₅ Thin Flakes, *Physical Review Letters*, 127 (2021) 237001.
- [11] H.W.S. Arachchige, W.R. Meier, M. Marshall, T. Matsuo, R. Xue, M.A. McGuire, R.P. Hermann, H. Cao, D. Mandrus, Charge Density Wave in Kagome Lattice Intermetallic ScV₆Sn₆, *Physical Review Letters*, 129 (2022) 216402.
- [12] S. Nie, J. Chen, C. Yue, C. Le, D. Yuan, Z. Wang, W. Zhang, H. Weng, Tunable Dirac semimetals with higher-order Fermi arcs in Kagome lattices Pd₃Pb₂X₂ (X=S, Se), *Sci. Bull.*, 67 (2022) 1958-1961.
- [13] A. Rüegg, G.A. Fiete, Fractionally charged topological point defects on the kagome lattice, *Phys. Rev. B*, 83 (2011) 165118.
- [14] W.-S. Wang, Z.-Z. Li, Y.-Y. Xiang, Q.-H. Wang, Competing electronic orders on Kagome lattices at van Hove filling, *Phys. Rev. B*, 87 (2013) 115135.
- [15] Z.-J. Cheng, I. Belopolski, H.-J. Tien, T.A. Cochran, X.P. Yang, W. Ma, J.-X. Yin, D. Chen, J. Zhang,

- C. Jozwiak, A. Bostwick, E. Rotenberg, G. Cheng, M.S. Hossain, Q. Zhang, M. Litskevich, Y.-X. Jiang, N. Yao, N.B.M. Schroeter, V.N. Strocov, B. Lian, C. Felser, G. Chang, S. Jia, T.-R. Chang, M.Z. Hasan, Visualization of Tunable Weyl Line in A–A Stacking Kagome Magnets, *Adv. Mater. (Weinheim, Ger.)*, 35 (2023) 2205927.
- [16] W. Ma, X. Xu, J.-X. Yin, H. Yang, H. Zhou, Z.-J. Cheng, Y. Huang, Z. Qu, F. Wang, M.Z. Hasan, S. Jia, Rare Earth Engineering in RMn_6Sn_6 (R=Gd-Tm, Lu) Topological Kagome Magnets, *Physical Review Letters*, 126 (2021) 246602.
- [17] S. Nakatsuji, N. Kiyohara, T. Higo, Large anomalous Hall effect in a non-collinear antiferromagnet at room temperature, *Nature*, 527 (2015) 212-215.
- [18] E. Liu, Y. Sun, N. Kumar, L. Muechler, A. Sun, L. Jiao, S.-Y. Yang, D. Liu, A. Liang, Q. Xu, J. Kroder, V. Stüß, H. Borrmann, C. Shekhar, Z. Wang, C. Xi, W. Wang, W. Schnelle, S. Wirth, Y. Chen, S.T.B. Goennenwein, C. Felser, Giant anomalous Hall effect in a ferromagnetic kagome-lattice semimetal, *Nature Physics*, 14 (2018) 1125-1131.
- [19] T. Kida, L.A. Fenner, A.A. Dee, I. Terasaki, M. Hagiwara, A.S. Wills, The giant anomalous Hall effect in the ferromagnet Fe_3Sn_2 —a frustrated kagome metal, *Journal of Physics: Condensed Matter*, 23 (2011) 112205.
- [20] M. Ikhlas, T. Tomita, T. Koretsune, M.-T. Suzuki, D. Nishio-Hamane, R. Arita, Y. Otani, S. Nakatsuji, Large anomalous Nernst effect at room temperature in a chiral antiferromagnet, *Nature Physics*, 13 (2017) 1085-1090.
- [21] X. Li, L. Xu, L. Ding, J. Wang, M. Shen, X. Lu, Z. Zhu, K. Behnia, Anomalous Nernst and Righi-Leduc Effects in Mn_3Sn : Berry Curvature and Entropy Flow, *Physical Review Letters*, 119 (2017) 056601.
- [22] X. Xu, J.-X. Yin, W. Ma, H.-J. Tien, X.-B. Qiang, P.V.S. Reddy, H. Zhou, J. Shen, H.-Z. Lu, T.-R. Chang, Z. Qu, S. Jia, Topological charge-entropy scaling in kagome Chern magnet TbMn_6Sn_6 , *Nature Communications*, 13 (2022) 1197.
- [23] H. Zhang, J. Koo, C. Xu, M. Sretenovic, B. Yan, X. Ke, Exchange-biased topological transverse thermoelectric effects in a Kagome ferrimagnet, *Nature Communications*, 13 (2022) 1091.
- [24] K. Kuroda, T. Tomita, M.T. Suzuki, C. Bareille, A.A. Nugroho, P. Goswami, M. Ochi, M. Ikhlas, M. Nakayama, S. Akebi, R. Noguchi, R. Ishii, N. Inami, K. Ono, H. Kumigashira, A. Varykhalov, T. Muro, T. Koretsune, R. Arita, S. Shin, T. Kondo, S. Nakatsuji, Evidence for magnetic Weyl fermions in a correlated metal, *Nature Materials*, 16 (2017) 1090-1095.
- [25] S. Peng, Y. Han, G. Pokharel, J. Shen, Z. Li, M. Hashimoto, D. Lu, B.R. Ortiz, Y. Luo, H. Li, M. Guo, B. Wang, S. Cui, Z. Sun, Z. Qiao, S.D. Wilson, J. He, Realizing Kagome Band Structure in Two-Dimensional Kagome Surface States of RV_6Sn_6 (R=Gd, Ho), *Physical Review Letters*, 127 (2021) 266401.
- [26] G. Pokharel, S.M.L. Teicher, B.R. Ortiz, P.M. Sarte, G. Wu, S. Peng, J. He, R. Seshadri, S.D. Wilson, Electronic properties of the topological kagome metals YV_6Sn_6 and GdV_6Sn_6 , *Phys. Rev. B*, 104 (2021) 235139.
- [27] Y. Hu, X. Wu, Y. Yang, S. Gao, N.C. Plumb, A.P. Schnyder, W. Xie, J. Ma, M. Shi, Tunable topological Dirac surface states and van Hove singularities in kagome metal GdV_6Sn_6 , *Sci. Adv.*, 8 (2022) eadd2024.
- [28] J.-X. Yin, W. Ma, T.A. Cochran, X. Xu, S.S. Zhang, H.-J. Tien, N. Shumiya, G. Cheng, K. Jiang, B. Lian, Z. Song, G. Chang, I. Belopolski, D. Multer, M. Litskevich, Z.-J. Cheng, X.P. Yang, B. Swidler, H. Zhou, H. Lin, T. Neupert, Z. Wang, N. Yao, T.-R. Chang, S. Jia, M. Zahid Hasan, Quantum-limit Chern

- topological magnetism in TbMn_6Sn_6 , *Nature*, 583 (2020) 533-536.
- [29] X. Teng, L. Chen, F. Ye, E. Rosenberg, Z. Liu, J.-X. Yin, Y.-X. Jiang, J.S. Oh, M.Z. Hasan, K.J. Neubauer, B. Gao, Y. Xie, M. Hashimoto, D. Lu, C. Jozwiak, A. Bostwick, E. Rotenberg, R.J. Birgeneau, J.-H. Chu, M. Yi, P. Dai, Discovery of charge density wave in a kagome lattice antiferromagnet, *Nature*, 609 (2022) 490-495.
- [30] J.-X. Yin, Y.-X. Jiang, X. Teng, M.S. Hossain, S. Mardanya, T.-R. Chang, Z. Ye, G. Xu, M.M. Denner, T. Neupert, B. Lienhard, H.-B. Deng, C. Setty, Q. Si, G. Chang, Z. Guguchia, B. Gao, N. Shumiya, Q. Zhang, T.A. Cochran, D. Multer, M. Yi, P. Dai, M.Z. Hasan, Discovery of Charge Order and Corresponding Edge State in Kagome Magnet FeGe , *Physical Review Letters*, 129 (2022) 166401.
- [31] D.M. Clatterbuck, K.A. Gschneidner, Magnetic properties of RMn_6Sn_6 ($\text{R}=\text{Tb, Ho, Er, Tm, Lu}$) single crystals, *Journal of Magnetism and Magnetic Materials*, 207 (1999) 78-94.
- [32] G. Venturini, B.C.E. Idrissi, B. Malaman, Magnetic properties of RMn_6Sn_6 ($\text{R} = \text{Sc, Y, Gd-Tm, Lu}$) compounds with HfFe_6Ge_6 type structure, *Journal of Magnetism and Magnetic Materials*, 94 (1991) 35-42.
- [33] J. Lee, E. Mun, Anisotropic magnetic property of single crystals RV_6Sn_6 ($\text{R}=\text{Y, Gd-Tm, Lu}$), *Phys. Rev. Materials*, 6 (2022) 083401.
- [34] H. Ishikawa, T. Yajima, M. Kawamura, H. Mitamura, K. Kindo, GdV_6Sn_6 : A Multi-carrier Metal with Non-magnetic 3d-electron Kagome Bands and 4f-electron Magnetism, *Journal of the Physical Society of Japan*, 90 (2021) 124704.
- [35] B.R. Ortiz, G. Pokharel, M. Gundayao, H. Li, F. Kaboudvand, L. Kautzsch, S. Sarker, J.P.C. Ruff, T. Hogan, S.J.G. Alvarado, P.M. Sarte, G. Wu, T. Braden, R. Seshadri, E.S. Toberer, I. Zeljkovic, S.D. Wilson, YbV_3Sb_4 and EuV_3Sb_4 vanadium-based kagome metals with Yb^{2+} and Eu^{2+} zigzag chains, *Phys. Rev. Materials*, 7 (2023) 064201.
- [36] L. Chen, Y. Zhou, H. Zhang, X. Ji, K. Liao, Y. Ji, Y. Li, Z. Guo, X. Shen, R. Yu, X. Yu, H. Weng, G. Wang, Tunable magnetism and electron correlation in Titanium-based Kagome metals RETi_3Bi_4 ($\text{RE} = \text{Yb, Pr, and Nd}$) by rare-earth engineering, 2023. arXiv:2307.02942
- [37] B. Malaman, G. Venturini, R. Welter, J.P. Sanchez, P. Vulliet, E. Ressouche, Magnetic properties of RMn_6Sn_6 ($\text{R}=\text{Gd-Er}$) compounds from neutron diffraction and Mössbauer measurements, *Journal of Magnetism and Magnetic Materials*, 202 (1999) 519-534.
- [38] G. Motoyama, M. Sezaki, J. Gouchi, K. Miyoshi, S. Nishigori, T. Mutou, K. Fujiwara, Y. Uwatoko, Magnetic properties of new antiferromagnetic heavy-fermion compounds, Ce_3TiBi_5 and CeTi_3Bi_4 , *Physica B: Condensed Matter*, 536 (2018) 142-144.
- [39] G. Pokharel, B. Ortiz, J. Chamorro, P. Sarte, L. Kautzsch, G. Wu, J. Ruff, S.D. Wilson, Highly anisotropic magnetism in the vanadium-based kagome metal TbV_6Sn_6 , *Phys. Rev. Materials*, 6 (2022) 104202.
- [40] E. Rosenberg, J.M. DeStefano, Y. Guo, J.S. Oh, M. Hashimoto, D. Lu, R.J. Birgeneau, Y. Lee, L. Ke, M. Yi, J.-H. Chu, Uniaxial ferromagnetism in the kagome metal TbV_6Sn_6 , *Phys. Rev. B*, 106 (2022) 115139.
- [41] C. Pfleiderer, S.R. Julian, G.G. Lonzarich, Non-Fermi-liquid nature of the normal state of itinerant-electron ferromagnets, *Nature*, 414 (2001) 427-430.
- [42] W.G. Baber, N.F. Mott, The contribution to the electrical resistance of metals from collisions between electrons, *Proceedings of the Royal Society of London. Series A - Mathematical and Physical Sciences*, 158 (1937) 383-396.
- [43] A.A. Abrikosov, I.M. Khalatnikov, Theory of the Fermi fluid (The Properties of Liquid He_3 at Low

Temperatures), Soviet Physics Uspekhi, 1 (1958) 68.

[44] A.H. Wilson, R.H. Fowler, The electrical conductivity of the transition metals, Proceedings of the Royal Society of London. Series A. Mathematical and Physical Sciences, 167 (1938) 580-593.

[45] N.F. Mott, Electrons in transition metals, Advances in Physics, 13 (1964) 325-422.

[46] X.-N. Luo, C. Dong, S.-K. Liu, Z.-P. Zhang, A.-L. Li, L.-H. Yang, X.-C. Li, Low-temperature physical properties and electronic structures of Ni_3Sb , Ni_5Sb_2 , NiSb_2 , and NiSb , Chin. Phys. B, 24 (2015) 067201.

[47] P.W. Phillips, N.E. Hussey, P. Abbamonte, Stranger than metals, Science, 377 (2022) eabh4273.

[48] J. Yuan, Q. Chen, K. Jiang, Z. Feng, Z. Lin, H. Yu, G. He, J. Zhang, X. Jiang, X. Zhang, Y. Shi, Y. Zhang, M. Qin, Z.G. Cheng, N. Tamura, Y.-f. Yang, T. Xiang, J. Hu, I. Takeuchi, K. Jin, Z. Zhao, Scaling of the strange-metal scattering in unconventional superconductors, Nature, 602 (2022) 431-436.

[49] X. Jiang, M. Qin, X. Wei, L. Xu, J. Ke, H. Zhu, R. Zhang, Z. Zhao, Q. Liang, Z. Wei, Z. Lin, Z. Feng, F. Chen, P. Xiong, J. Yuan, B. Zhu, Y. Li, C. Xi, Z. Wang, M. Yang, J. Wang, T. Xiang, J. Hu, K. Jiang, Q. Chen, K. Jin, Z. Zhao, Interplay between superconductivity and the strange-metal state in FeSe, Nature Physics, 19 (2023) 365-371.

[50] N.W.a.M. Ashcroft, N.D., Solid State Physics, Saunders College, Philadelphia, 1976.

[51] H. Chen, J. Gao, L. Chen, G. Wang, H. Li, Y. Wang, J. Liu, J. Wang, D. Geng, Q. Zhang, J. Sheng, F. Ye, T. Qian, L. Chen, H. Weng, J. Ma, X. Chen, Topological crystalline insulator candidate ErAsS with hourglass Fermion and magnetic-tuned topological phase transition, Adv. Mater. (Weinheim, Ger.), DOI 10.1002/adma.202110664(2022) 2110664.

[52] Y. Li, E. Wang, X. Zhu, H.-H. Wen, Pressure-induced superconductivity in Bi single crystals, Phys. Rev. B, 95 (2017) 024510.

Supporting Information for Publication

**Anisotropic and pressure tunable magnetism of titanium-based Kagome ferromagnet
 SmTi_3Bi_4**

Long Chen (陈龙)^{1,2,#}, Ying Zhou (周颖)^{1,2,#}, He Zhang (张赫)^{1,2,#}, Zhongnan Guo (郭中楠)³,
Xiaohui Yu (于晓辉)^{1,2,4,*}, Gang Wang (王刚)^{1,2,4,*}

¹ Beijing National Laboratory for Condensed Matter Physics, Institute of Physics, Chinese
Academy of Sciences, Beijing 100190, China

² University of Chinese Academy of Sciences, Beijing 100049, China

³ Department of Chemistry, School of Chemistry and Biological Engineering, University of
Science and Technology Beijing, Beijing 100083, China

⁴ Songshan Lake Materials Laboratory, Dongguan, Guangdong 523808, China

These authors contributed equally to this work.

*Corresponding author. Email: yuxh@iphy.ac.cn; gangwang@iphy.ac.cn.

Supplementary Note 1: Materials and methods.

Single Crystal Growth. SmTi₃Bi₄ single crystals were grown by a high-temperature solution method using Bi as flux [1]. The as-received Sm ingot (Alfa, 99.9%) was cut into small pieces, then mixed with Ti powder (99.95%, Alfa Aesar) and Bi granules (99.999%, Sinopharm) with a molar ratio of Sm : Ti : Bi = 2 : 4 : 12 in a fritted alumina crucible set (Canfield crucible set) [2] and sealed in a fused-silica ampoule at vacuum. The ampoule was heated to 1073 K over 15 h, held at the temperature for 24 h, and then slowly cooled down to 873 K at a rate of 2 K/h. At 873 K, hexagonal-shaped, shiny-silver single crystals with size up to 5 mm × 5 mm × 0.5 mm were separated from the remaining liquid by centrifuging the ampoule. Considering the possible air sensitivity of the surface, all manipulations and specimen preparation for structure characterization and property measurements were handled in an argon-filled glove box.

Structure Characterization and Composition Analysis. X-ray diffraction data were obtained using a PANalytical X'Pert PRO diffractometer (Cu K_{α} radiation, $\lambda = 1.54178 \text{ \AA}$) operated at 40 kV voltage and 40 mA current with a graphite monochromator in a reflection mode ($2\theta = 5^{\circ}$ – 100° , step size = 0.017°). Indexing and Rietveld refinement were performed using the DICVOL91 and FULLPROF programs [3]. Single crystal X-ray diffraction (SCXRD) data were collected using a Bruker D8 VENTURE with Mo K_{α} radiation ($\lambda = 0.71073 \text{ \AA}$) at 280 K for SmTi₃Bi₄. The structure was solved using a direct method and refined with the Olex2 [4] and Jana2020 [5] package. The morphology and chemical composition were characterized using a scanning electron microscope (SEM-4800, Hitachi) equipped with an electron microprobe analyzer for semiquantitative elemental analysis in energy-dispersive spectroscopy (EDS) mode. Three spots in different areas were measured on each crystal using EDS.

Physical Property Measurements. Temperature-dependent magnetic susceptibility were measured using a vibrating sample magnetometer system (VSM, Quantum Design) under a magnetic field (0.5 T) parallel ($H // bc$) and perpendicular ($H \perp bc$) to the bc plane using both the zero-field-cooling and field-cooling protocols. Only magnetic susceptibility in FC protocol was measured under a larger field (1 T), and the field-dependent magnetization curves were measured under the magnetic field up to 7 T parallel and perpendicular to the bc plane. The resistivity and heat capacity measurements were carried out using a physical property measurement system (Quantum Design, 9 T). The resistivity was measured using the standard four-probe configuration with the applied current (about 2 mA) parallel to the bc plane. Heat capacity measurement was carried out at temperature ranging from 2.2 K to 200 K at high vacuum (0.01 μbar). To protect the sample from air and moisture, thin film of N-type grease ($\sim 0.05 \text{ mg}$) was spread to cover the sample in an argon-filled glove box, then the sample was mounted on the square plate of specialized heat capacity puck in air.

Supplementary Note 2: Crystal structure and chemical composition.

Table S1. Crystallographic data and structure refinement of SmTi₃Bi₄.

Empirical formula	SmTi ₃ Bi ₄	
f.u. weight (g/mol)	1129.97	
Space group / Z	<i>Fmmm</i> (No.69) / 4	
Unit cell parameter	<i>a</i> (Å)	24.900(4)
	<i>b</i> (Å)	10.3371(16)
	<i>c</i> (Å)	5.8863(9)
	α, β, γ (°)	90
	<i>V</i> (Å ³)	1515.1(4)
<i>d</i> _{cal} (g/cm ³)	4.954	
Refl. Collectd / unique	2997 / 535	
<i>R</i> _{int}	0.0570	
Goodness-of-fit	1.126	
<i>R</i> ₁ / <i>wR</i> ₂ (<i>I</i> > 2σ(<i>I</i>))	0.1025 / 0.3321	
<i>R</i> ₁ / <i>wR</i> ₂ (all)	0.1068 / 0.3418	

Table S2. Atomic coordinates and equivalent isotropic displacement parameters for SmTi₃Bi₄.

Atom	Wyck.	Sym.	<i>x/a</i>	<i>y/b</i>	<i>z/c</i>	Occ.	<i>U</i> (eq)(Å ²)
Sm	8 <i>g</i>	2 <i>mm</i>	0.6958(2)	0.5000	0	1.0	0.0101(11)
Ti1	8 <i>g</i>	<i>m</i>	0.5933(4)	0.5000	0.5000	1.0	0.0060(20)
Ti2	16 <i>l</i>	<i>m</i>	0.5961(3)	0.2500	0.2500	1.0	0.0052(17)
Bi1	8 <i>h</i>	<i>m</i>	0.5000	0.3306(2)	0.5000	1.0	0.0061(9)
Bi2	16 <i>o</i>	<i>m</i>	0.6889(1)	0.3399(2)	0.5000	1.0	0.0068(9)
Bi3	8 <i>g</i>	<i>m</i>	0.5691(1)	0.5000	0	1.0	0.0063(9)

Table S3. Anisotropic displacement parameters for SmTi₃Bi₄. The anisotropic displacement factor exponent takes the form: $-2\pi^2[h^2a^2U_{11} + \dots + 2hkabU_{12}]$.

Atom	<i>U</i> ₁₁ (Å ²)	<i>U</i> ₂₂ (Å ²)	<i>U</i> ₃₃ (Å ²)	<i>U</i> ₂₃ (Å ²)	<i>U</i> ₁₃ (Å ²)	<i>U</i> ₁₂ (Å ²)
Sm	0.0053(17)	0.0034(18)	0.0220(30)	0	0	0
Ti1	0.0240(60)	0.0160(50)	-0.0220(50)	0	0	0
Ti2	0.0090(40)	0.0060(40)	0.0010(40)	0	0	0.0010(30)
Bi1	0.0083(15)	0.0043(14)	0.0055(17)	0	0	0
Bi2	0.0047(13)	0.0029(13)	0.0127(17)	0.0008(5)	0	0
Bi3	0.0034(13)	0.0029(13)	0.0126(18)	0	0	0

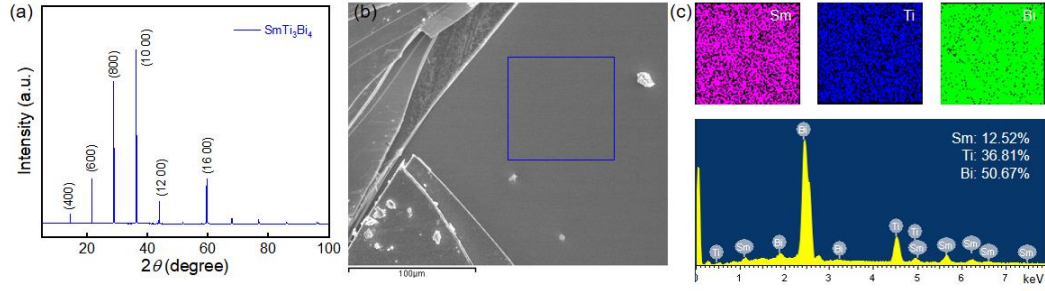


Figure S1. Crystal structure and chemical composition. (a) X-ray diffraction pattern of an as-grown SmTi_3Bi_4 single crystal, showing (00 l) ($l = \text{even integers}$) diffraction peaks. (b) SEM image of SmTi_3Bi_4 at a scale of 100 μm . (c) Elemental mapping and elemental analysis by EDS, showing the homogenous distribution of Sm, Ti, and Bi.

Table S4. Quantitative analysis of chemical composition for SmTi_3Bi_4 single crystals. For each sample, the molar ratio of composed elements is measured at three different locations. The final stoichiometry of SmTi_3Bi_4 is determined to be Sm : Ti : Bi = 0.95(3) : 3.00(6) : 4.16(6) by the statistical average and standard deviation (SD) of the overall EDS data.

Atom	Sm (mol%)	Ti (mol%)	Bi (mol%)
SA#-1	11.66	35.30	53.04
SA#-2	11.79	36.61	51.60
SA#-3	11.79	37.30	51.59
SB#-1	11.74	37.33	50.93
SB#-2	11.18	38.02	50.80
SB#-3	11.90	36.79	51.31
SC#-1	12.20	37.79	50.41
SC#-2	11.59	36.80	51.62
SC#-3	11.95	37.59	50.46
Average	11.68	37.01	51.31
SD	0.35	0.78	0.80

Supplementary Note 3: Magnetism and specific heat capacity.

Table S5. Fitted parameters of magnetic susceptibility for SmTi_3Bi_4 using Curie-Weiss law.

Field configuration	$H // a$	$H // b$	$H // c$
χ_0 (10^{-4} emu mol $^{-1}$ Oe $^{-1}$)	0.36(1)	2.29(6)	-6.50(4)
C (10^{-3} emu mol $^{-1}$ Oe $^{-1}$ K $^{-1}$)	9.59(5)	3.11(2)	1.68(5)
θ (K)	0.55(1)	0.55(1)	2.50(1)
μ_{eff} ($\mu_B/\text{f.u.}$)	0.28(1)	0.16(1)	3.66(5)
μ_{sat} ($\mu_B/\text{f.u.}$)	0.016	0.006	1.620

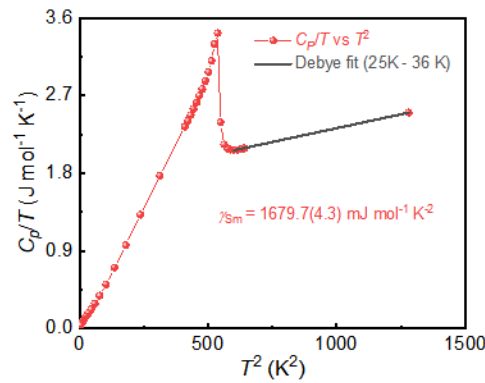


Figure S2. Debye fitting beyond T_c . C_p/T vs T^2 plot and corresponding fitting (black lines) using Debye model at high temperature (25 K - 36 K).

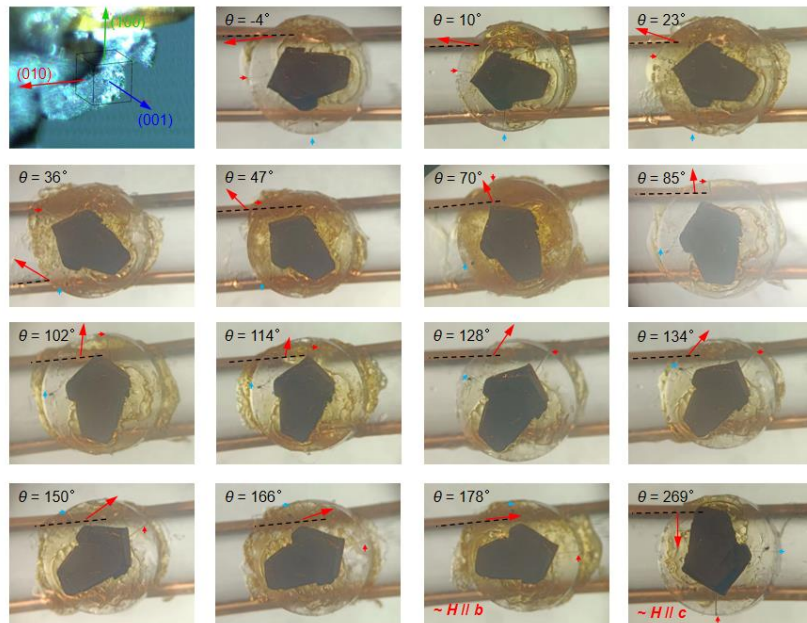


Figure S3. Crystal orientation and measurement configurations for in-plane magnetic anisotropy of SmTi_3Bi_4 single crystal. Crystal orientation of SmTi_3Bi_4 single crystals was carried out on a Bruker D8 VENTURE with Mo K_α radiation ($\lambda = 0.71073\text{\AA}$) at 300 K. The orientated crystal was first attached on a nonmagnetic quartz plate with the b axis almost along the direction

of the magnetic field ($\theta = -4^\circ$). By rotating the quartz plate, the angle between the b axis and in-plane magnetic field would change.

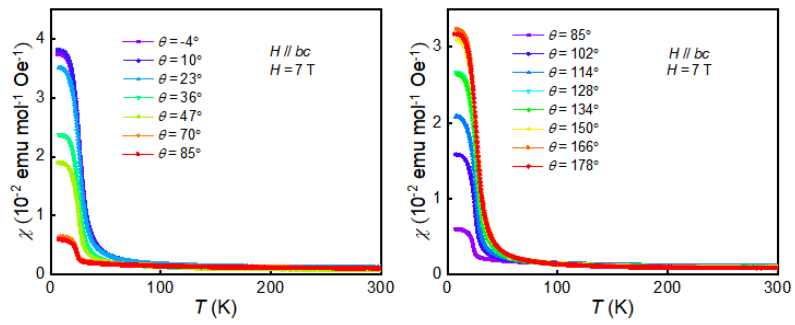


Figure S4. In-plane magnetic anisotropy of SmTi_3Bi_4 single crystal. Temperature-dependent magnetic susceptibility of SmTi_3Bi_4 under large in-plane magnetic field (7 T) with θ ranging from (a) -4° to 85° and (b) 85° to 178° .

Supplementary Note 4: Resistance at high pressure.

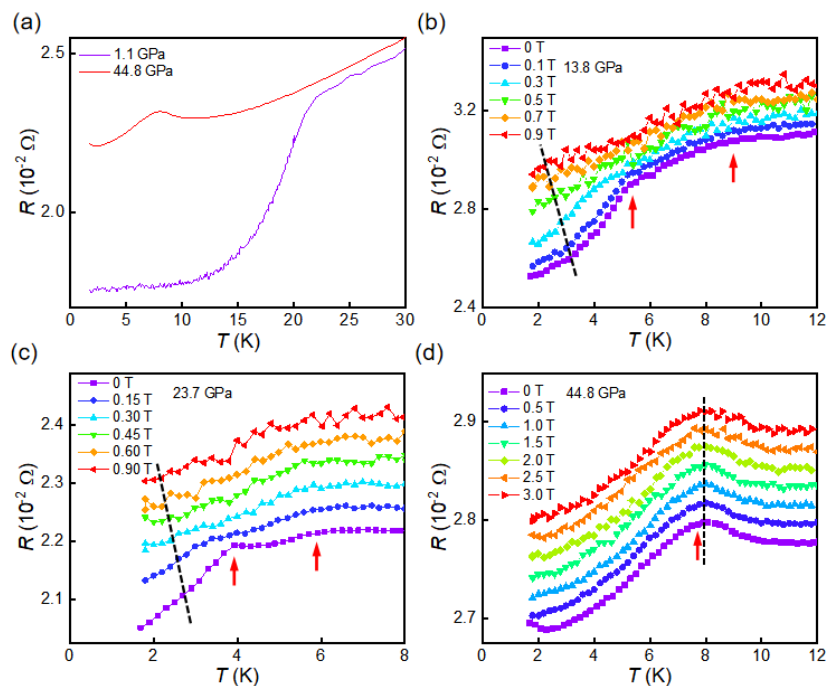


Figure S5. Resistance at high pressure of SmTi_3Bi_4 . (a) Comparison of the resistance under 1.1 GPa and 44.8 GPa for SmTi_3Bi_4 . The evolution of resistance with external magnetic field under (b) 13.8 GPa, (c) 23.7 GPa, and (d) 44.8 GPa. The arrows and dashed lines denote the position of ordering temperatures and its evolution trend.

- [1] L. Chen, Y. Zhou, H. Zhang, X. Ji, K. Liao, Y. Ji, Y. Li, Z. Guo, X. Shen, R. Yu, X. Yu, H. Weng, G. Wang, Tunable magnetism and electron correlation in Titanium-based Kagome metals RETi_3Bi_4 (RE = Yb, Pr, and Nd) by rare-earth engineering, 2023.
- [2] P.C. Canfield, T. Kong, U.S. Kaluarachchi, N.H. Jo, Use of frit-disc crucibles for routine and exploratory solution growth of single crystalline samples, *Philosophical Magazine*, 96 (2016) 84-92.
- [3] J. Rodríguez-Carvajal, FullProf, CEA/Saclay, France, DOI (2001).
- [4] O.V. Dolomanov, L.J. Bourhis, R.J. Gildea, J.A.K. Howard, H. Puschmann, OLEX2: a complete structure solution, refinement and analysis program, *J. Appl. Crystallogr.*, 42 (2009) 339-341.
- [5] V. Petříček, M. Dušek, L. Palatinus, Crystallographic Computing System JANA2006: General features, *Zeitschrift für Kristallographie - Crystalline Materials*, 229 (2014) 345-352.